

Efficiency calibration for in vivo measurement of Pb-210 in the skull using phantoms developed for Chinese adult reference male*

Xiang-Peng Meng,^{1,2,3} Yuan-Yuan Liu,^{2,3,4,5,†} Bin Wu,^{2,3,4,5,‡} Yu Wang,^{2,3,4,5} Jing Wang,^{2,3,4,5} Lai Zhou,^{2,3,4,5} Ao Ju,^{2,3,4,5} Yun-Shi Xiao,⁶ Qin-Jian Cao,⁶ Zhi Zeng,¹ Qian Yue,¹ and Jian-Ping Cheng^{2,3,4,5}

¹Department of Engineering Physics, Tsinghua University, Beijing, 100084, China

²Jinping Deep Underground Frontier Science and Dark Matter Key Laboratory of Sichuan Province, 615000, China

³Joint Laboratory of Jinping Ultra-low Radiation Background Measurement of

Ministry of Ecology and Environment Beijing Normal University, 100875, China

⁴School of Physics and Astronomy, Beijing Normal University, Beijing, 100875, China

⁵Key Laboratory of Beam Technology of Ministry of Education, 100875, China

⁶China Institute for Radiation Protection, Taiyuan, 030006, China

Efficiency calibration is a critical step that enables the conversion of the detectors' count rate into the activity of radionuclides in the examined parts for in vivo measurement. However, to date, there hasn't been a well-accepted framework for efficiency calibration. As such, it is often found researchers employ various kinds of anthropomorphic phantoms with considerably different patterns of radionuclide distribution coupling with drastically different numbers of detectors to derive the calibration factor, rendering the cross-comparison among studies challenging. Moreover, some studies employ virtual calibration, whereas others prefer experimental calibration, though their equivalency has not been fully explored. In this paper, focusing on in vivo measurement of Pb-210 in the skull, a promising technique for individualized reconstruction of radon exposure is presented, and a detailed framework for efficiency calibration covering key issues mentioned above is provided. To be specific, physical phantoms of Pb-210 in the skull are developed based on the anatomical characteristics of a Chinese adult reference male, along with the corresponding computational phantoms constructed from computed tomography scan. In comparison, the average deviations between simulation and experimental results are within 4% for efficiency calibration at the top, left, and right sides of the head across varying detection distances. Furthermore, based on the investigation of Pb-210 distribution regions reported in literature, the calculation method for Pb-210 activity is improved to account for different source distributions and joint measurements with multiple detectors. The results are useful for determining the appropriate conversion procedure under different measurement conditions.

Keywords: Radon, Pb-210, in vivo measurement, efficiency calibration

I. INTRODUCTION

The skeleton is one of the primary targeting organs for screening contamination within the human body. Bone-seeking radionuclides can accumulate in the volume or on the surface of the skeleton[1–6]. In this context, the skeleton is often regarded as a “dosimeter” [7], as the activity of the radionuclides deposited in the bone can be used to estimate the dose resulting from their presence. For example, radon is the second leading cause of lung cancer, next only to smoking[8–10]. Pb-210, as a decay product of radon, can uniformly distribute and reside in the skeleton, characterizing long physical and biological half-lives of 22.2 years and 10 years, respectively[3, 11, 12]. Researchers are developing a cutting-edge method to reconstruct radon exposure through the in vivo measurement of Pb-210 in the skeleton, thereby helping to establish the relationship between radon exposure and lung cancer risk[1–3, 5, 7, 13–24].

The instruments used for in vivo measurements mainly consist of the detector array and the shielding room[25, 26]. Since Pb-210 in the skeleton emits gamma rays of 46.5 keV

that can exit out of the body, it can be monitored externally using the gamma-ray detector. The skull has the largest surface area among all bones, accounting for 13~15% of the total skeletal mass[23]. Thus, measuring Pb-210 activity in the skull enables estimation of that in the whole skeleton. Additionally, the upper epidermis of the skull is relatively thin, which reduces the attenuation of radiation caused by the self-absorption of body tissues. Therefore, the skull is the optimal detection position for in vivo measurement of Pb-210[1].

Calibrating the counting efficiency of detectors for characteristic γ -rays using anthropomorphic phantoms is a crucial step in the measurement process. These phantoms, composed of human tissue-equivalent materials, resemble the shape, size, and attenuation characteristics of the subjects being measured and contain a known activity of target radionuclides. Since Eisenbud et al.[3] conducted the first in vivo measurement of Pb-210 in the skull in 1969, researchers have developed various skull phantoms containing Pb-210 over the past half-century. For example, Dantas et al.[2]constructed two physical skull phantoms for measuring Brazilian coal miners, one with a uniform distribution of 2755 Bq on the inner surface of the skull, and the other with 2581 Bq on the outer surface. However, the physical skull phantoms developed to date are primarily based on the characteristics of Caucasians, which can lead to significant errors when applied to Chinese individuals. Consequently, in 1992, Zheng et al.[24]first fabricated a skull phantom suitable for Chinese

* Supported by the National Natural Science Foundation of China (No. 12222502).

[†] Corresponding author, E-mail: yyliu@bnu.edu.cn

[‡] Corresponding author, E-mail: bwu6@bnu.edu.cn

individuals by averaging the skulls of 80 Chinese cadavers. Nonetheless, the dimensions and other details of the phantom are sparsely described, making it difficult to trace. Therefore, an important aspect of this work is the development of physical skull phantoms for Chinese reference male.

Furthermore, to ensure the accuracy of efficiency calibration, it is necessary to establish a library of phantoms that reflects distinct anatomical characteristics across various individuals. However, the fabrication of high-fidelity physical phantoms is laborious and costly. Fortunately, recent advancements in medical imaging and computational technology provide a viable alternative, allowing for the construction of computational phantoms through Computed Tomography (CT) or Magnetic Resonance Imaging (MRI) scans. Combined with the Monte Carlo method, simulations can account for the complete process of the interaction between radiation and the phantom[27]. Computational phantoms have several advantages over physical ones, such as the ability to characterize higher anatomical fidelity with the resolution of mm or even smaller[28, 29]. Moreover, computational phantoms are completely non-radioactive, ensuring absolute safety for operators. Source-free efficiency calibration methods have been widely applied in vivo measurement of internal contamination with radionuclides, such as Am-241[4, 6, 30–32]. Given the similarities between Pb-210 and Am-241, both bone-seeking radionuclides with close characteristic γ -ray energies (Am-241, 59.5 keV), the virtual calibration method should also be applicable to Pb-210 in vivo measurement. Although computational phantoms are convenient and flexible to use, there are very few studies in the literature that use virtual calibration of Pb-210 in the skull for in vivo measurement. Therefore, the work will conduct a study on the virtual calibration method, aiming to take advantages of computational phantoms while also validating accuracy of the method.

The efficiency calibration factor (in cps/Bq), which represents the full-energy peak count of the target nuclide with unit activity per second in the gamma detector, can be calculated by measuring the γ -rays emitted by phantoms with known activity. This factor is related to the solid angle of the detector relative to the source, the γ -ray emission probability, and the self-attenuation of these rays in matter[33–42]. After calibrating the efficiency using phantoms, the activity is calculated by dividing the counting rate from measured subject by the derived efficiency calibration factor. However, it is found that this conversion procedure was inadequately described in the literature, which may raise two questions: First, the methods of source distribution differ among studies, leading to different definitions of the efficiency calibration factor. For example, both the skull cap and the whole skull are common areas where Pb-210 is distributed within the skull phantom, resulting in efficiency calibration factors representing two distinct definitions. Since the efficiency calibration mimics the measurement conditions, the region of the test subject corresponding to the calculated Pb-210 activity aligns with the area of source distribution. Therefore, results under different source distribution areas cannot be directly compared. Second, studies commonly employ multiple detectors, which increase the surface area to enhance the solid angle of

the detectors with respect to the skull, thereby improving detection efficiency. In the scenario of joint measurement with multiple detectors, researchers usually treat all detectors as a whole, where the activity is equal to the total count rate divided by overall efficiency calibration factor. However, this method may not be optimal for calculating activity, as it treats all detector results as equally important. In fact, variations in detector type, measurement position, and detection distance lead to differences in counting efficiency between detectors. Moreover, because the Pb-210 in the skull has low activity, its detection can be easily affected by background. As a result, the uncertainty of the results varies across different detectors, with one or more detectors possibly showing relatively high uncertainty. Simply summing the count rates from these detectors could lead to suboptimal uncertainty in the final result, or even increase it. Therefore, this suggests the need to develop a method to improve the conversion procedure and minimize uncertainty in the results.

The purpose of the present work is to perform the efficiency calibration of Pb-210 in the skull, based on physical and computational skull phantoms developed for the Chinese reference male. In this work, CT scanning is used to construct computational phantoms, and virtual efficiency calibration is carried out by combining the Monte Carlo method. The accuracy of the method will be verified by comparing the results between the experiment and simulation. Moreover, the calculation method for the Pb-210 activity in the skull will be improved under different distribution regions of the source, along with joint measurements using multiple detectors.

II. MATERIALS AND METHODS

A. Fabrication of the skull phantom

1. Dimension

The present work focuses on Chinese adult reference male, aged 20 to 50 years, who measures 170 cm in height and weighs 63 kg, according to the "Reference individuals for use in radiation protection" standard (GBZ/T 200.1-2007)[43]. The size parameters of the head are defined as follows: circumference 57 cm (measured from the point between the eyebrows, around the back of the head to the starting point), length 19 cm (the straight-line distance from the point between the eyebrows to the back of the head), height 23 cm (the vertical distance from the top of the head to the point under the chin), and breadth 16 cm (the distance between the left and right sides of the skull), as shown in Figure 1. According to ICRP Publication 145[44], the Caucasian reference male phantom has a height of 176 cm and a weight of 73 kg. Because the report provides a 3D model without specifying the size parameters of the head, the phantom is measured using software. The length, height, and breadth of the head are 21.4 cm, 21.6 cm, and 15.1 cm, respectively. In comparison, the maximum relative bias in head dimensions between the Chinese and Caucasian reference phantoms is about 11%.

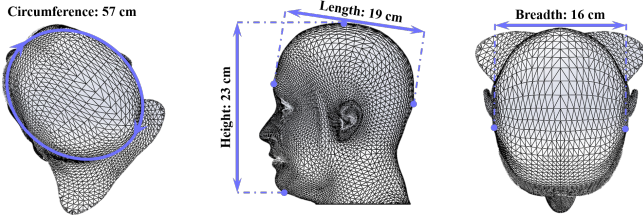


Fig. 1. The size parameters of head for the Chinese reference adult male phantom.

2. Distribution of Pb-210 in the skull

Referring to related studies, the most common method of Pb-210 distribution involves uniform placement on both the inner and outer surfaces of the skull or skull cap. Similarly, in this study, the source is uniformly distributed on the surface of the skull cap, resulting in two skull phantoms containing Pb-210. One phantom has the source on its inner surface with an activity of 4270 Bq, and the other on its outer surface with an activity of 4200 Bq, as shown in Figure 2(a). In the figure, the green and blue regions represent the inner and outer surface distributions in the skull, respectively.

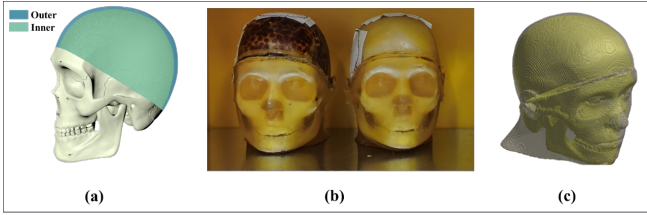


Fig. 2. The sketches depict the setup of Pb-210 distribution, as well as physical and computational skull phantoms. (a) The Pb-210 distribution setup, with green and blue representing Pb-210 placed on the inner and outer surfaces of the skull, respectively; (b) physical skull phantoms containing source placements on the outer and inner surfaces, shown on the left and right sides, respectively; (c) the computational skull phantom.

3. Materials

Despite the diversity and complexity of head tissues and organs, which Iacono et al.[35] reported to include around 100 types, many head organs or tissues have similar densities. Therefore, to reduce the laboriousness and costs of production, researchers often use one material to substitute for multiple tissues or organs when preparing equivalent materials. According to reports from International Commission on Radiological Protection (ICRP) Publications 23, 110, and International Commission on Radiation Units and Measurements (ICRU) Report 46[46–48], the main organs or tissues of the head include the brain, muscles, blood vessels, the central nervous system, soft tissues, and the skeleton, as shown in Table 1. Except for bones, the densities of these tissues

are closely aligned, with a bias of less than 3% from the soft tissue density of 1.03 g/cm^3 , as reported in the ICRU 46 Report[48]. Thus, the construction of head organs and tissues is simplified by substituting all tissues except for the bone with soft tissue. Finally, the structure of the phantom consists of soft tissue and bone, with reference densities of 1.03 g/cm^3 and 1.40 g/cm^3 , respectively. In collaboration with the Chinese Institute for Radiation Protection (CIRP), two physical skull phantoms containing Pb-210 are designed and fabricated, as depicted in Figure 2(b). The densities of the soft tissue and bone used are 1.08 g/cm^3 and 1.38 g/cm^3 , respectively, with a relative bias less than 5% from the reference values. Additionally, physical skull phantoms are transformed into voxel computational phantoms through CT scanning, as illustrated in Figure 2(c), with voxel dimensions of $0.78125 \text{ mm} \times 0.78125 \text{ mm} \times 1 \text{ mm}$. The number of voxels for the outer and inner source distributions of the phantoms is $219 \times 260 \times 237$ and $218 \times 258 \times 240$, respectively.

TABLE 1. The density of main tissues or organs in the head.

Head tissues	Density (g/cm^3)	Reference
Brain	1.05	ICRP 110[47]
Muscle	1.05	ICRP 110[47]
Blood vessels	1.06	ICRP 110[47]
Central nervous system	1.04	ICRP 23[46]
Soft tissues	1.03	ICRU 46[48]
Skeleton	1.40	ICRP 23[46]

B. Conditions of experiment and simulation

1. Experiment setup

The efficiency calibration experiment for Pb-210 in the skull is conducted in the Whole Body Counter (WBC) device at Beijing Normal University (BNU) in Beijing, China. The shielding room of the WBC is composed of 15 cm-thick low-background steel. The detector array used in the WBC consists of three HPGe detectors, as shown in Figure 3(a). Two HPGe BE6530 detectors are placed on the left and right sides of the phantom, and one HPGe BE5030 detector is positioned at the top of the phantom. The detection distance should not be set too far from phantom due to the relatively low detection efficiency of Pb-210. Therefore, the detection distance is set to a range of 0~5 cm, with a step size of 1 cm for each detector movement. The detection distance represents the shortest distance from the detector window to the surface of the skull phantom. A measurement time of 3600 s is sufficient, yielding a statistical uncertainty in counts within 1.3%. The calibration measurements were performed on two physical skull phantoms containing Pb-210 on the inner or outer surface. The results are derived from the geometric mean of

calibration factors from both phantoms.

2. Simulation setup

The Monte Carlo tool used in simulation is Geant4[49–51], version 10.0.3, which is a powerful software capable of simulating radiation transport and energy deposition. To verify the accuracy of the virtual calibration, the simulation conditions in Geant4 must mimic the experimental setup as closely as possible. Therefore, detection scenario is configured to align with the experiment, as depicted in Figure 3(b). Based on the parameters provided by the manufacturer, the model of the HPGe detectors is shown in Figure 3(b). The green region represents the sensitive volume (Ge crystal) of the detector. The crystal diameter distinguishes the HPGe BE5030 from the BE6530, with D_{5030} being 8.05 cm for the former and D_{6530} being 9.12 cm for the latter. This work implements the import of the voxel computational phantom using the DICOM program provided in Geant4. The DICOM program requires files of definition in the g4dcm format, which specify the material composition, density, and voxel dimensions of the phantom. A MATLABTM program has been developed to generate g4dcm files describing the voxel computational phantom in Geant4[52]. The simulation used Pb-210 γ -rays at 46.5 keV, with 5×10^6 sources uniformly distributed on both the inner or outer surfaces of the skull. Figure 3(c) illustrates the detector positions on both sides and the top of the head in relation to the phantom. The red circle with a cross denotes the detector center.

III. RESULTS AND DISCUSSION

A. Comparison of simulation and experiment

Based on the setup described in Section 2, Figure 4 presents experimental and simulation results for Pb-210 efficiency calibration in the skull at detection distances from 0 to 5 cm, in 1 cm increments. The absolute value of the relative uncertainty for each point representing the calibration factor is within 1%. Figure 4(a), (b), and (c) show the detector positioned on the left, right, and top of the phantom, respectively. Hollow and solid points represent the results of the experiment and simulation, respectively. In the Geant4 world, the model of the voxel computational phantom is constructed inside a rectangular box, which prevents the detectors from penetrating it and avoids boundary overlap. For measurements at the top of the head, where the highest point of phantom meets the rectangular box boundary, detectors can closely approach the head, achieving a minimum detection distance of 0 cm. However, for measurements on both sides of the phantom, where the edges of the ears align with the box boundaries, detectors cannot directly contact the surface of phantom. Hence, the minimum measurement distance on the left and right sides is set to 1 cm in simulation. The results suggest that the average bias between the results of simulation and experiment for the left, right, and top of the head is

0.66%, 1.14%, and 3.88%, respectively, at detection distances from 0 to 5 cm. The simulation and experimental results for the detectors placed on both sides of the head, except for the top, are in the order of counting uncertainty. An important reason for the relatively large bias in the results at the top of the head is that the top detector moves differently from the left and right detectors when the detection distance changes. Although the top detector is carefully moved manually, unlike the left and right detectors, which are mechanically moved and more precise, this could cause slight deviations from the expected path. Therefore, when the simulation and experimental conditions are same, the virtual efficiency calibration of Pb-210 in the skull can achieve high accuracy.

Furthermore, the results show that the calibration factors at the three measurement positions approximately exhibit a linear relationship with the detection distance. With each 1 cm increase in detection distance, the efficiency calibration factor decreases by approximately 14%. When the detection distance increases from 0 to 5 cm, the efficiency calibration factor is reduced to $\sim 50\%$ of its original value. In addition, the detectors positioned on the left and right sides of the head, as well as at the top, have different surface areas. Given the significant correlation between the efficiency calibration factor and the surface area of the detector, the efficiency calibration factors are normalized to the surface area for a fair comparison across different positions, as shown in Figure 5. The square, circle, and triangle markers represent the efficiency calibration factors $v/Area$ normalized by the detector surface area for the left and right sides of the head and the top, respectively. It can be observed that the average relative bias of $v/Area$ for both sides of the head is about 5% for a detection distance of 0 to 5 cm, indicating good symmetry in the physical skull phantom. Among the three measurement positions, the efficiency calibration factor per unit detector surface area is highest at the top of the head for the same detector distance; here, it exceeds the average for the left and right sides of the head by approximately 22% and 28%, respectively.

B. Calculation method of Pb-210 activity in the skull

1. Derivation of the formula

The key role of the efficiency calibration factor is to convert the count rate of the detector into activity A as follows[53, 54]:

$$A = \frac{n}{v} \quad (1)$$

where n represents the count per second detected by the detector, and v represents the efficiency calibration factor. Since the conditions of calibration and measurement are the same, the region of the source distribution represented by the efficiency calibration factor in Equation (1) corresponds to the skull area of the test subject, where the Pb-210 activity is to be calculated. Following the review and reanalysis of the reported results in the literature[1–3, 5, 7, 13–24], the distribution regions of Pb-210 vary across studies. These can

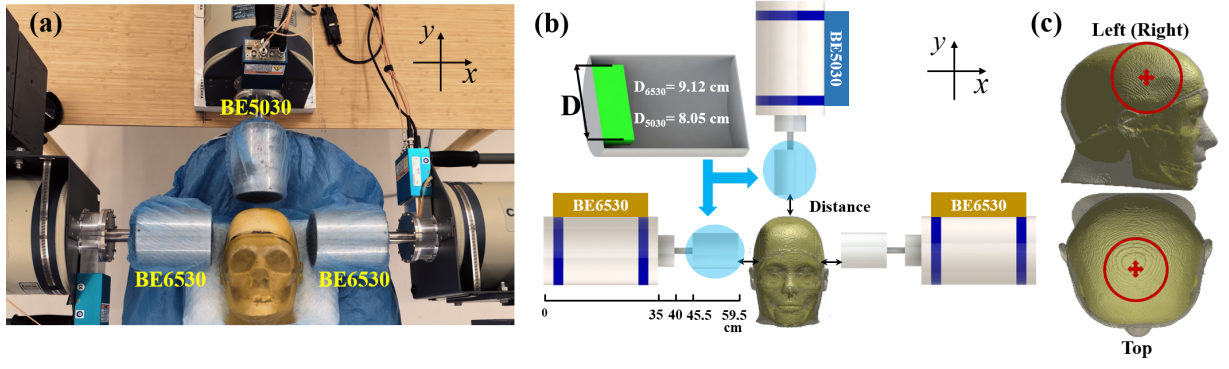


Fig. 3. Schematic illustration of the experiment and simulation in efficiency calibration. (a) Experiment, where two HPGe BE6530 detectors are placed on both sides and an HPGe BE5030 detector on top; (b) simulation, where the green region represents the probe crystal. HPGe BE5030 is characterized by a crystal diameter D_{5030} of 8.00 cm, while for HPGe BE6530, the corresponding dimension, D_{6530} , is 9.12 cm; (c) red circles denote the relative positions of left (right) and top detectors, with crosses representing the detector centers.

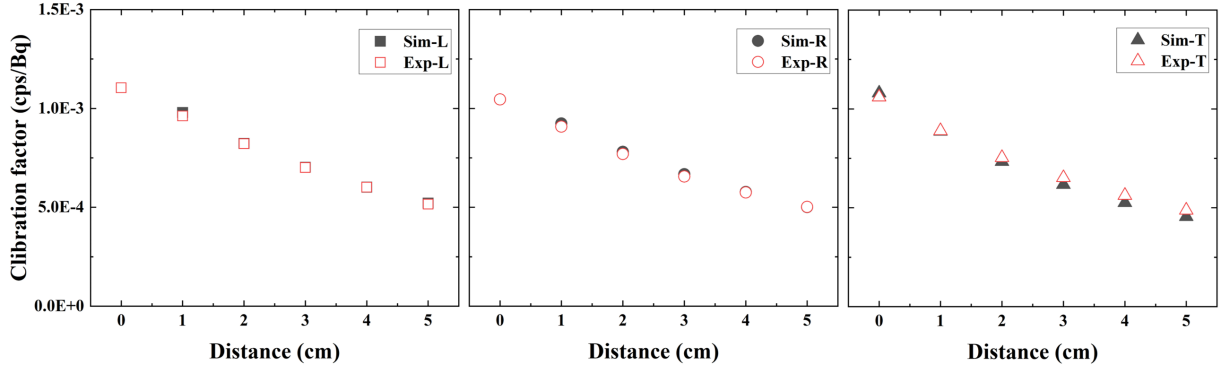


Fig. 4. The calibration factor of Pb-210 in the skull is illustrated, where (a), (b), and (c) represent the placement of detectors on the left, right, and top of the phantom, with detector distances ranging from 0 to 5 cm, respectively. Hollow and solid points represent the results of the experiment and simulation, respectively. “Sim” and “Exp” refer to simulation and experiment, respectively. “L”, “R” and “T” denote the detectors placed on the left, right, and top of the head, respectively.

be classified into three types based on their characteristics: “Half”, “Skull-cap”, and “Full”, as illustrated in Figure 6. “Half” refers to sourcing on half of the skull with the nasal midline as the axis of symmetry; “Skull-cap” represents the source placed in the cap region of the skull; and “Full” indicates the source is distributed in the entire skull. The distribution region of Pb-210 determines the position of the detectors, which are confined to the skull region containing the source. In this case, the efficiency calibration factor represents the count rate contributed to the detector by the unit activity of Pb-210 within the source placement region. To calculate the Pb-210 activity in the skull, it is necessary to consider the proportion of the source distribution region within the skull. Therefore, Equation (1) can be improved as follows:

$$A_{Skull} = \frac{n}{v} \cdot \frac{1}{\eta} \quad (2)$$

where η represents the percentage of the mass in the skull occupied by the source region, and A_{Skull} denotes the activity of Pb-210 in the skull. The use of Equation (2) includes an assumption[19]: there is no contribution to the detector’s

count if Pb-210 source is also distributed outside the region of efficiency calibration. The validity of this assumption lies in the weak penetration ability of Pb-210 gamma rays. While the area of the subject beyond the calibration region, corresponding to that of the phantom, can emit gamma rays, this radiation is easily attenuated by body tissues and the detector casing. Therefore, the count contribution primarily originates from the area inside the region directly covered by detectors positioned very close to the head.

Furthermore, researchers often employ multiple detectors for joint measurements of Pb-210 activity in the skull, with the types of detectors including phoswich and HPGe detectors, as indicated in the second column of Table 2[1–3, 5, 13, 15, 23, 24]. It can be found that the phoswich detector, which comprises stacked NaI and CsI scintillators and can operate in an anticoincidence mode, was commonly used before the 21st century. However, in recent years, the HPGe detector with high energy resolution has often been employed. Based on relevant studies and prior research[17], it has been demonstrated that both types of detectors have equivalent detection capabilities for Pb-210. The calibration factor de-

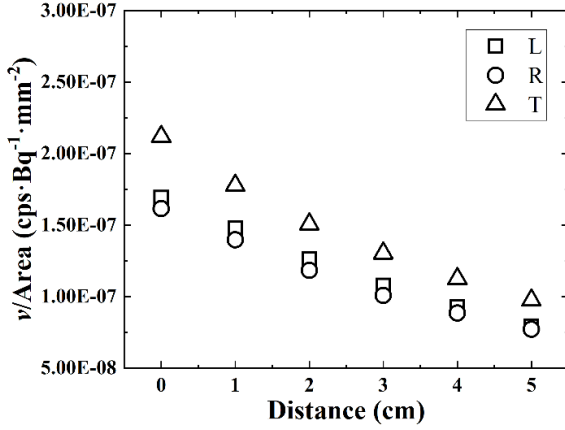


Fig. 5. $v/Area$ represents the efficiency calibration factors normalized by the detector surface area. The square, circle, and triangle symbols represent the normalized efficiency calibration factors for the left, right, and top of the phantom, respectively. “L”, “R”, and “T” denote the measurement position on the left, right, and top of the head, respectively.

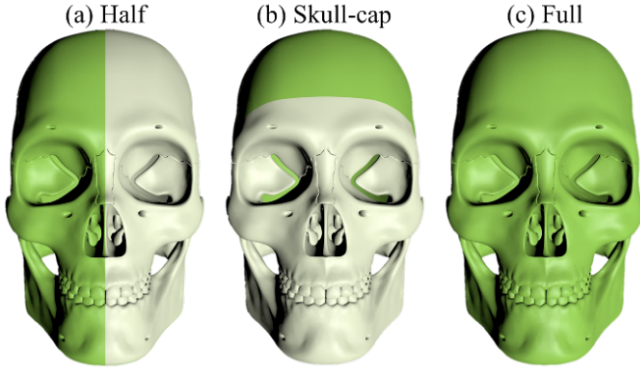


Fig. 6. The distribution regions of Pb-210 in the skull. The green represents the distribution region of Pb-210, while white represents the region without source. (a) “Half” refers to sourcing on half of the skull along the nasal midline; (b) “Skull-cap” represents Pb-210 distributed in the cap of the skull; (c) “Full” indicates that the entire skull is covered by the source.

pendes on the detector’s surface area rather than its type. Thus, the detection efficiency can be enhanced by using multiple detectors, specifically by increasing the surface area to cover a larger solid angle of the head. The third and fourth columns of Table 2 list the number of detectors and their surface area used by each research institute. It can be seen that although there are fewer phoswich detectors compared to HPGe detectors, the surface area of a phoswich detector is larger than that of an HPGe detector. The former is approximately six times that of the latter when dividing the total surface area by the total number of detectors. When multiple detectors are used to measure Pb-210 in the skull, researchers commonly regard all detectors as a whole. Therefore, this means that the total

efficiency calibration factor is the sum of the factors for each detector. Using this method (referred to as the “summation method” below), the total count rate is the sum of count rates from each detector. This allows the calculation of Pb-210 activity A_{Skull}^+ in the skull using Equation (3) as follows:

$$A_{Skull}^+ = \frac{\sum_i^j n_i}{\sum_i^j v_i} \cdot \frac{1}{\eta} \quad (3)$$

where n_i the count per second of detector i , v_i denotes the efficiency calibration factor of detector i , and j refers to the number of detectors used. This method assumes that results of all detector are equal importance. However, differences in detector types, measurement positions, and detection distances lead to varying counting efficiencies across detectors. Additionally, the Pb-210 in the skull has a low activity level, making its detection more susceptible to background interference. Consequently, the uncertainties of the results differ between detectors, with some detectors possibly having relatively high uncertainty. Simply summing the count rates from these detectors can result in suboptimal uncertainty in the final outcome, or even worsen it. Therefore, the activity calculation method should be improved.

TABLE 2. The type, number, and surface area of detectors are derived from different studies. The first column lists the reference literature, while the second, third, and fourth columns represent the type, number, and total surface area of the detectors used in studies, respectively.

References	Detector		
	Type	Number	Area (mm ²)
Eisenbud et al. (1969)[3]	Phoswich	1	32429
Cohen et al. (1973)[13]	Phoswich	2	36483
Cohen et al. (1977)[1]	Phoswich	3	54724
Zheng et al. (1992)[24]	Phoswich	1	12272
Estrada et al. (1993)[15]	Phoswich	3	54724
Wahl et al. (2000)[23]	HPGe	7	24400
Haninger et al. (2002)[5]	HPGe	4	15703
Dantas et al. (2007)[2]	HPGe	4	8000

2. Improvement of calculation method

To discuss the improvement of the calculation method for Pb-210 in the skull, the measurement system used in this work is employed to explain how efficiency calibration factors for the joint measurement of multiple detectors can be applied to calculate Pb-210 activity in the skull, as shown in

Figure 7. Figure 7(a) shows the scene for efficiency calibration, where cylinders represent detectors, red curves depict gamma rays, and the ellipsoid with a shadow denotes the skull phantom, with the shaded region indicating the placement of the source in the skull cap region. v_1 , v_2 , and v_3 represent the efficiency calibration factors for detectors placed on the left, right, and top of the head, respectively. Figure 7(b) shows the measurement of Pb-210 in the skull of subject, where n_1 , n_2 , and n_3 denote the count rates contributed by Pb-210 with detectors placed on the left, right, and top of the head, respectively. When using the summation method for calculation, the

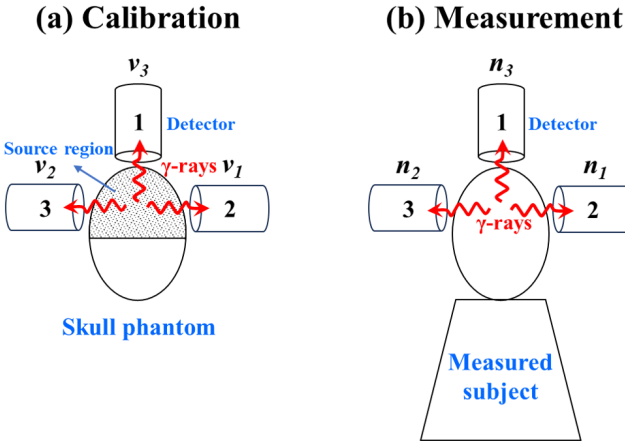


Fig. 7. Schematic diagram of the joint measurement with multiple detectors. (a) Efficiency calibration; (b) Measurement of the subject. Cylinders represent detectors, red curves represent gamma rays, and the ellipsoid with a shadow represents the skull phantom, where the shaded area represents the distribution of the source in the skull. v_1 , v_2 , and v_3 represent the efficiency calibration factors for detectors on the left, right, and top of the skull phantom, respectively. n_1 , n_2 , and n_3 denote the counts per second contributed by Pb-210, with detectors placed on the left, right, and top of the head, respectively.

activity of Pb-210 in the skull and its relative uncertainty can be expressed as follows:

$$A_{Skull}^+ = \frac{n_1 + n_2 + n_3}{(v_1 + v_2 + v_3)} \cdot \frac{1}{\eta}, \quad \sigma_{A_{Skull}^+} = \frac{\sqrt{\sigma_1^2 + \sigma_2^2 + \sigma_3^2}}{n_1 + n_2 + n_3} \quad (4)$$

where $\sigma_{A_{Skull}^+}$ and $\frac{\sigma_{A_{Skull}^+}}{A_{Skull}^+}$ represent the absolute and relative uncertainties, respectively; σ_1 , σ_2 , and σ_3 denote the uncertainties of the result from detectors placed on the left, right, and top of the head, respectively.

Since the summation method treats all detector results as equally important, and some detectors may show relatively higher uncertainty, summing the count rates from these detectors can result in suboptimal uncertainty in the final outcome, or even worsen it. In this case, the weighted mean method can be used to compute the Pb-210 activity in the skull. In this approach, each of the three detectors is treated as independently measuring, allowing the activity of Pb-210 in the skull to be calculated separately for each detector using Equation

(2). Theoretically, the results using the three detectors should be identical; however, there can be variation among the results from each detector. This is due to the relatively low activity of Pb-210 and the impracticality of setting excessively long measurement times for the test person, resulting in low counts with significant statistical uncertainty. Thus, to reduce the uncertainty in the results, and following the core concept of the weighted mean, different weights can be assigned to the results from the three detectors based on their uncertainties. Thus, the calculation of Pb-210 in the skull can be expressed as follows:

$$\bar{A}_{Skull} = (w_1 \frac{n_1}{v_1} + w_2 \frac{n_2}{v_2} + w_3 \frac{n_3}{v_3}) \cdot \frac{1}{\eta}, \quad w_1 + w_2 + w_3 = 1, 0 < w_1, w_2, w_3, \quad \sigma_{\bar{A}_{Skull}} = \frac{\sqrt{(\frac{w_1}{v_1})^2 \sigma_1^2 + (\frac{w_2}{v_2})^2 \sigma_2^2 + (\frac{w_3}{v_3})^2 \sigma_3^2}}{(\frac{w_1}{v_1} n_1 + \frac{w_2}{v_2} n_2 + \frac{w_3}{v_3} n_3)} \quad (5)$$

where w_1 , w_2 , and w_3 represent the weights of the measurement results from the detectors placed on the left, right, and top of the head, respectively. These weights are normalized to one and assigned based on the uncertainty of the results. $\sigma_{\bar{A}_{Skull}}$ and $\frac{\sigma_{\bar{A}_{Skull}}}{\bar{A}_{Skull}}$ represent the absolute and relative uncertainties, respectively.

For the relative uncertainty to be minimized, assuming $f(w_1, w_2, w_3) = \frac{\sigma_{\bar{A}_{Skull}}}{\bar{A}_{Skull}}$, w_1 , w_2 , and w_3 should satisfy $\frac{\partial f}{\partial w_1} = 0$, $\frac{\partial f}{\partial w_2} = 0$, $\frac{\partial f}{\partial w_3} = 0$. Meanwhile, the Hessian matrix should be a positive definite matrix as follows:

$$H(f) = \begin{pmatrix} \frac{\partial^2 f}{\partial w_1^2} & \frac{\partial^2 f}{\partial w_1 \partial w_2} & \frac{\partial^2 f}{\partial w_1 \partial w_3} \\ \frac{\partial^2 f}{\partial w_2 \partial w_1} & \frac{\partial^2 f}{\partial w_2^2} & \frac{\partial^2 f}{\partial w_2 \partial w_3} \\ \frac{\partial^2 f}{\partial w_3 \partial w_1} & \frac{\partial^2 f}{\partial w_3 \partial w_2} & \frac{\partial^2 f}{\partial w_3^2} \end{pmatrix}, \quad X^T H(f) X > 0 \quad (6)$$

where $H(f)$ represents the Hessian matrix, and X refers to the any non-zero vector. By solving the equations mentioned above, the weight factor for each detector can be determined for calculating the Pb-210 activity in the skull. For instance, in an experiment measuring Pb-210 in the skull of a normal person with detection distance of 0 cm, the counts per second of the detectors placed on the left, right and top of the head are $0.96 \pm 1.30 \times 10^{-3}$ cps, $1.45 \pm 1.14 \times 10^{-3}$ cps, $2.22 \pm 0.63 \times 10^{-3}$ cps, respectively. The uncertainty in the above results primarily comes from background interference and the low counts because of the low Pb-210 activity in the skull of a normal person. The relative uncertainties for detectors positioned on the left, right, and top of the head are 135.41%, 78.62%, and 28.38%, respectively. If the summation method is used for calculation, the relative uncertainty of the result is 39.75%. The results suggest that the relative uncertainty using the summation method is higher than that of the top detector, which is due to the high uncertainty of the results from the detectors on both sides of the head. In contrast, when w_1 , w_2 , and w_3 are 0.08, 0.15, and 0.77, respectively, the relative uncertainty of the result is minimized to 26.19%. Hence, the result obtained through the weighted mean method is more precise than that derived from the sum-

mation method. Additionally, it can be found that the detector with the lower uncertainty is assigned a larger weight factor. Furthermore, if w_1 , w_2 , and w_3 are set to $v_1/(v_1 + v_2 + v_3)$, $v_2/(v_1 + v_2 + v_3)$, and $v_3/(v_1 + v_2 + v_3)$, respectively, for minimizing the relative uncertainty, substituting these values into Equation (5) transforms it into Equation (4). In this case, the summation method and the weighted mean method are equivalent.

IV. SUMMARY

In this work, a study is conducted on the method of efficiency calibration for Pb-210 in the skull based on the developed physical and computational skull phantom of the Chinese adult reference male. With detection distances ranging from 0 to 5 cm, the average bias between the calibration factors from simulation and experiment is all within 4% for detectors placed on the left, right, and top of the phantom. The results suggest that the method of virtual efficiency calibration has good accuracy for Pb-210 in the skull. Moreover, it is found that the calibration factors decreased by approximately 14% with each 1 cm increase in detection distance for detectors positioned on both sides and the top of the phantom. It is noteworthy that, at the same detection distance, the calibration factor for the top of the phantom is approximately

22% and 28% higher than that for left and right sides, respectively. Therefore, if only one detector is available for the measurement, it is recommended to place it on the top of the head.

Furthermore, by combining the analysis of reported data in the literature, the conversion method for Pb-210 activity in the skull is discussed, reflected in two aspects: on one hand, the distribution region of Pb-210 differs among studies when fabricating the physical skull phantom, leading to variations in the efficiency calibration factor. This work derives a calculation method for Pb-210 activity in the skull, considering the different distribution regions of the source. On the other hand, in multi-detector measurements, the summation method (i.e., combining count rates from multiple detectors) is commonly used in research. However, if one of the detectors has significant measurement uncertainty, simply summing the count rates from these detectors can result in suboptimal uncertainty in the final outcome, or even worsen it. Therefore, the weighted mean method is derived, assigning weights to each detector to minimize the relative uncertainty of the results, which makes it more precise than the summation method for calculating Pb-210 activity.

These studies would help promote the realization of in vivo measurements of Pb-210 in the skull to assess the risk of lung cancer resulting from chronic radon exposure.

-
- [1] N. Cohen, H.B. SPITZ, M.E. WRENN, Estimation of skeletal burden of "bone-seeking" radionuclides in man from in vivo scintillation measurements of the head. *Health Phys.* **33**, 431-441 (1977). [doi:10.1097/00004032-197711000-00009](https://doi.org/10.1097/00004032-197711000-00009)
 - [2] A.L. Dantas, B.M. Dantas, J.L. Lipsztein, et al., In vivo measurements of ^{210}Pb in skull and knee geometries as an indicator of cumulative ^{222}Rn exposure in a underground coal mine in Brazil. *Radiat Prot Dosimetry*, **125**, 568-571 (2007). [doi:10.1093/rpd/ncl387](https://doi.org/10.1093/rpd/ncl387)
 - [3] M. Eisenbud., G.R. LAURER., J.C. ROSEN., et al., In vivo measurement of lead-210 as an indicator of cumulative radon daughter exposure in uranium miners. *Health Phys.* **16**, 637-646 (1969). [doi:10.1097/00004032-196905000-00011](https://doi.org/10.1097/00004032-196905000-00011)
 - [4] K. Fantínová, P. Fojtík, V. Pfeiferová, A whole body counter for an emergency and occupational monitoring of an internal contamination with low energy photon emitters. *Radiat. Phys. Chem.* **116**, 160-164 (2015). [doi:10.1016/j.radphyschem.2015.05.005](https://doi.org/10.1016/j.radphyschem.2015.05.005)
 - [5] T. Haninger, W. Wahl, L. Salonen, et al., In vivo measurements on the human skull for retrospective assessment of individual intakes of natural radionuclides. *Int. Congr.* **1225**, 95-100 (2002). [doi:10.1016/S0531-5131\(01\)00539-8](https://doi.org/10.1016/S0531-5131(01)00539-8)
 - [6] P. Nogueira, W. Ruhm, Person-specific calibration of a partial body counter used for individualised ^{241}Am skull measurements. *J. Radiol. Prot.* **40**, 1362-1389 (2020). [doi:10.1088/1361-6498/abbe36](https://doi.org/10.1088/1361-6498/abbe36)
 - [7] G.R. Laurer., J.J.S. Estrada., N. Cohen., Lung exposure from inhalation of radon progeny calculated from in vivo measurements of Pb-210 in the skull, *Health Phys.* **76**, 380-387 (1999). [doi:10.1097/00004032-199904000-00005](https://doi.org/10.1097/00004032-199904000-00005)
 - [8] World Health Organization (WHO), *Handbook on indoor radon: a public health perspective*. (WHO, Geneva, 2009), pp. 1-91
 - [9] W.G. Li, D.T. Xiao, Z.Z. He, et al., Reference device for calibration of radon exhalation rate measuring instruments and its performance. *Nucl. Sci. Tech.* **34** (2023). [doi:10.1007/s41365-023-01275-3](https://doi.org/10.1007/s41365-023-01275-3)
 - [10] M. Xia, Y.J. Ye, S.Y. Liu, et al., Numerical simulations for radon migration and exhalation behavior during measuring radon exhalation rate with closed-loop method. *Nucl. Sci. Tech.* **35** (2024). [doi:10.1007/s41365-024-01362-z](https://doi.org/10.1007/s41365-024-01362-z)
 - [11] J. Wang, Y.Y. Liu, B. Wu, et al., Theoretical prediction of the ^{210}Pb burden in the skeleton from radon exposure and other intake routes. *Health Phys.* **127**, 287-297 (2024). [doi:10.1097/HP.0000000000001807](https://doi.org/10.1097/HP.0000000000001807)
 - [12] Y. Wang, Y.Y. Liu, B. Wu, et al. Measurement on specific activity of ^{210}Pb and ^{40}K in tea and tobacco via low background high purity germanium gamma spectrometer. *Atom. Energy Sci. Technol.* **57**, 1048-1056 (2023). (in Chinese)
 - [13] N. Cohen, T. Jaakkola, M.E. Wrenn, Lead-210 concentrations in the bone, blood and excreta of a former uranium miner. *Health Phys.* **24**, 601-609 (1973). [doi:10.1097/00004032-197306000-00001](https://doi.org/10.1097/00004032-197306000-00001)
 - [14] A.L.A. Dantas, B.M. Dantas, J.L. Lipsztein, et al., A method for analyzing low statistics high resolution spectra from Pb-210 in underground coal miners from Brazil, *J. Radioanal. Nucl. Chem.* **269**, 435-459 (2007). [doi:10.1007/s10967-006-0404-2](https://doi.org/10.1007/s10967-006-0404-2)
 - [15] J.J.S. Estrada, G.R. Laurer, A method to obtain subject background for low-level In vivo measurements of the head. *Health Phys.* **65**, 306-312 (1993). [doi:10.1097/00004032-199309000-00010](https://doi.org/10.1097/00004032-199309000-00010)
 - [16] G. Laurer., Q.T. Gang, G.H. Lubin, et al., Skeletal ^{210}Pb

- levels and lung cancer among radon-exposed tin miners in southern China. *Health Phys.* **64**, 253-259 (1993). doi:10.1097/00004032-199303000-00003
- [17] X.P. Meng, Y. Liu, B. Wu et al., Minimum detectable activity of Pb-210 in skull from in vivo measurements: insights from the literature. *Front. Energy Res.* **9**, 759850 (2021). doi:10.3389/fenrg.2021.759850
- [18] X.P. Meng, Y. Liu, B. Wu et al., Assessment of radiation background suppression using phoswich detectors for in vivo Pb-210 measurements: A simulation study. *Nucl. Technol.* **208**, 753–760 (2021). doi:10.1080/00295450.2021.1945358
- [19] X.P. Meng, Y.Y. Liu, B. Wu, et al., Virtual calibration for in vivo measurement of Pb-210 activity in the skull using BOMAB, MIRD, and MIDA phantoms. *Appl. Radiat. Isot.* **205**, 111192 (2024). doi:10.1016/j.apradiso.2024.111192
- [20] M. Muikku, T. Rahola, S. Pusa, et al., Estimation of human exposure to natural radionuclides using in vivo skull measurements. *Radiat. Prot. Dosim.* **105**, 615-618 (2003). doi:10.1093/oxfordjournals.rpd.a006313
- [21] I. Pillalamarri, P. Jagam, G.I. Lykken, Internal dosimetry of ^{210}Pb in the human cranium: preliminary results from instrumentation needs for in vivo counting in a low-background underground counting facility. *Radiat. Prot. Dosim.* **157**, 6-10 (2013). doi:10.1093/rpd/nct109
- [22] R. Scheler, K. Dettmann, J. Brose, Retrospective estimation of exposure to short-lived ^{222}Rn progeny by measurements of ^{210}Pb in the skull. *Radiat. Prot. Dosim.* **79**, 129-132 (1998). doi:10.1093/oxfordjournals.rpd.a032375
- [23] W. Wahl, T. Haninger, D. Kucheida, et al., Study of long-term radon progeny in humans for retrospective evaluation of radon exposure. *J. Radioanal. Nucl. Chem.* **243**, 447-450 (2000). doi:10.1023/A:1016078115609
- [24] R.Q. Zheng, S.L. Wang, R.W. Ma, et al., Skull ^{210}Pb Content measurement and lung dose estimation from radon progeny of tin miners. *Radiat. Prot. Bull.* 45-53 (1992). (in Chinese)
- [25] Y. Wang, Y.Y. Liu, B. Wu, et al., Experimental investigation on the radiation background inside body counters. *Nucl. Sci. Tech.* **33** (2022). doi:10.1007/s41365-022-01004-2
- [26] Y. Wang, Y.Y. Liu, B. Wu, et al., Reconstruction of indoor gamma-ray background spectrum for HPGe detectors. *Radiat. Meas.* **174**, 107139 (2024). doi:10.1016/j.radmeas.2024.107139
- [27] X.Y. Luo, R. Qiu, Z. Wu, et al., THUDosePD: a three-dimensional Monte Carlo platform for phantom dose assessment. *Nucl. Sci. Tech.* **34** (2023). doi:10.1007/s41365-023-01315-y
- [28] X.G. Xu, An exponential growth of computational phantom research in radiation protection, imaging, and radiotherapy: a review of the fifty-year history. *Phys. Med. Biol.* **59**, R233-302 (2014). doi:10.1088/0031-9155/59/18/R233
- [29] J.H. Wang, R. Qiu, Z. Wu, et al., Normalized glandular dose coefficients for digital breast tomosynthesis using detailed Chinese breast models. *Nucl. Sci. Tech.* **35** (2024). doi:10.1007/s41365-024-01396-3
- [30] P. Nogueira, W. Rühm, M.A. Lopez, EURADOS 241Am skull measurement intercomparison. *Radiat. Meas.* **82**, 64-73 (2015). doi:10.1016/j.radmeas.2015.07.011
- [31] T. Vrba, D. Broggio, M. Caldeira, et al., EURADOS intercomparison exercise on MC modelling for the in-vivo monitoring of AM-241 in skull phantoms (Part II and III). *Radiat. Phys. Chem.* **113**, 59-71 (2014). doi:10.1016/j.radphyschem.2015.04.009
- [32] T. Vrba, P. Nogueira, D. Broggio, et al., EURADOS intercomparison exercise on MC modeling for the in-vivo monitoring of Am-241 in skull phantoms (Part I). *Radiat. Phys. Chem.* **104**, 332-338 (2014). doi:10.1016/j.radphyschem.2013.12.010
- [33] M.S. Badawi, M.M. Gouda, S.S. Nafee, et al., New algorithm for studying the effect of self attenuation factor on the efficiency of γ -rays detectors, *Nucl. Instrum. Meth. A.* **696**, 164-170 (2012). doi:10.1016/j.nima.2012.08.089
- [34] M.S. Badawi, M.M. Gouda, S.S. Nafee, et al., New analytical approach to calibrate the co-axial HPGe detectors including correction for source matrix self-attenuation, *Appl. Radiat. Isot.* **70**, 2661-2668 (2012). doi:10.1016/j.apradiso.2012.08.014
- [35] M.S. Badawi, M. Abd-Elzaher, A.A. Thabet, et al., An empirical formula to calculate the full energy peak efficiency of scintillation detectors, *Appl. Radiat. Isot.* **74**, 46-49 (2013). doi:10.1016/j.apradiso.2012.12.011
- [36] A.M. El-Khatib, M.M. Gouda, M.S. Badawi, et al., New analytical approach to calibrate the NaI (TI) detectors using spherical radioactive sources, *Radiat. Prot. Dosim.* **156**, 109-117 (2013). doi:10.1093/rpd/nct048
- [37] M.S. Badawi, I. Ruskov, M.M. Gouda, et al., A numerical approach to calculate the full-energy peak efficiency of HPGe well-type detectors using the effective solid angle ratio, *9*, P07030 (2014). doi:10.1088/1748-0221/9/07/P07030
- [38] M.S. Badawi, A numerical simulation method for calculation of linear attenuation coefficients of unidentified sample materials in routine gamma ray spectrometry, *Nucl. Technol. Radiat. Prot.* **30**, 249-259 (2015). doi:10.2298/NTRP1504249B
- [39] M.M. Gouda, M.S. Badawi, A.M. El-Khatib, et al., Calibration of well-type NaI(Tl) detector using a point sources measured out the detector well at different axial distances, *J. Instrum.* **10**, P03022 (2015). doi:10.1088/1748-0221/10/03/P03022
- [40] A.M. El-Khatib, M.S. Badawi, A.A. Thabet, et al., Well-type NaI(Tl) detector efficiency using analytical technique and ANGLE 4 software based on radioactive point sources located out the well cavity, *Chin. J. Phys.* **54**, 338-346 (2016). doi:10.1016/j.cjph.2016.03.019
- [41] M. Elsafi, J.S. Alzahrani, M.I. Abbas, et al., Geant4 tracks of NaI cubic detector peak efficiency, including coincidence summing correction for rectangular sources, *Nucl. Sci. Eng.* **195**, 1008-1016 (2021). doi:10.1080/00295639.2021.1895406
- [42] M.S. Badawi, A. Thabet, Analytical computation technique for calculation the effective geometrical solid angle and the efficiency of cubic scintillation crystal with side cylindrical hole, *Nucl. Technol. Radiat. Prot.* **37**, 91-102 (2022). doi:10.2298/NTRP2202091B
- [43] Ministry of Health of the People's Republic of China, *Reference individuals for use in radiation protection Part 1: Physique parameters*. (People's Health Publishing House, Beijing, 2006), pp.1-4
- [44] International Commission on Radiological Protection (ICRP), Adult mesh-type reference computational phantoms, ICRP Publication 145. *Ann. ICRP.* **49**, 1-203 (2020).
- [45] M.I. Iacono, E. Neufeld, E. Akinnagbe, et al., MIDA: a multimodal imaging-based detailed anatomical model of the human head and neck. *PLoS One.* **10**, e0124126 (2015). doi:10.1371/journal.pone.0124126
- [46] International Commission on Radiological Protection (ICRP), *Report on the task group on reference man*. (Pergamon Press, Oxford, 1975), pp. 1-467.
- [47] International Commission on Radiological Protection, Adult reference computational phantoms, ICRP Publication 110. *Ann. ICRP.* **39**, 1-165 (2009).

- [48] International Commission on Radiation Units and Measurements (ICRU), *Photon, electron, proton and neutron interaction data for body tissues*. (ICRU, Bethesda, 1992), pp. 1-206.
- [49] S. Agostinelli, J. Allison, K. Amako, et al., Geant4—a simulation toolkit. *Nucl. Instrum. Methods A*. **506**, 250-303 (2003). doi:10.1016/S0168-9002(03)01368-8
- [50] J. Allison, K. Amako, J. Apostolakis, et al., Geant4 developments and applications. *IEEE T. Nucl. Sci.* **53**, 270–278 (2006). doi:10.1109/TNS.2006.869826
- [51] J. Allison, K. Amako, J. Apostolakis, et al., Recent developments in Geant4. *Nucl. Instrum. Methods A*. **835**, 186–225 (2016). doi:10.1016/j.nima.2016.06.125
- [52] X.P. Meng, Y.Y. Liu, B. Wu, et al., Importing high-fidelity MIDA phantom into Geant4 for calibrating in vivo measurement of internal radioactivity, *2022 IEEE Nuclear Science Symposium and Medical Imaging Conference (NSS/MIC)* (Milano, Italy, 5–12 Nov. 2022)
- [53] M.S. Rahman, A.S. Mollah, A. Begum, et al., Body radioactivity and radiation dose from ^{40}K in Bangladeshi subjects measured with a whole-body counter, *Radiat. Prot. Dosim.* **130**, 236-238 (2007). doi:10.1093/rpd/ncm501
- [54] M.T. Taha, T. Morsi, Estimation of the total body burden for some individuals using whole body counter, *J. Radiat. Res. Appl. Sci.* **15**, 353-356 (2022). doi:10.1016/j.jrras.2022.08.007